# Wavelength Tunability of Ion-bombardment Induced Ripples on Sapphire

Hua Zhou, Yiping Wang, Lan Zhou, and Randall L. Headrick\*

Department of Physics, University of Vermont, Burlington, VT 05405 USA

Ahmet S. Özcan, Yiyi Wang, Gözde Özaydin, and Karl F. Ludwig Jr. Department of Physics, Boston University. MA 02215 USA

# D. Peter Siddons

National Synchrotron Light Source,

Brookhaven National Laboratory, Upton, NY 11973 USA

(Dated: July 27, 2021)

# Abstract

A study of ripple formation on sapphire surfaces by 300 - 2000 eV Ar<sup>+</sup> ion bombardment is presented. Surface characterization by *in-situ* synchrotron grazing incidence small angle x-ray scattering and *ex-situ* atomic force microscopy is performed in order to study the wavelength of ripples formed on sapphire (0001) surfaces. We find that the wavelength can be varied over a remarkably wide range – nearly two orders of magnitude – by changing the ion incidence angle. Within the linear theory regime, the ion induced viscous flow smoothing mechanism explains the general trends of the ripple wavelength at low temperature and incidence angles larger than 30°. In this model, relaxation is confined to a few-nm thick damaged surface layer. The behavior at high temperature suggests relaxation by surface diffusion. However, strong smoothing is inferred from the observed ripple wavelength near normal incidence, which is not consistent with either surface diffusion or viscous flow relaxation.

PACS numbers: 68.35.Bs, 61.10.Eq, 81.16.Rf, 81.65.Cf

## I. INTRODUCTION

Energetic particle bombardment on surfaces is known to produce one-dimensional (ripples or wires) and zero-dimensional (dot) structures at the submicron or nano-scale by a self-organization process. Recently, significant experimental and theoretical effort has been expended in order to develop ion bombardment patterning methods for the production of periodic nanostructures on various substrates.<sup>1,2,3,4,5,6,7,8</sup> These studies have demonstrated the potential to tailor surface morphology and related surface properties for novel optoelectronic and spintronic applications.<sup>9,10</sup> In addition, recent work has provided new insight into the mechanisms of the instability-driven self-organization process.<sup>11</sup>

A significant milestone in our understanding of the origins of a self-organized ripple topography formed by ion sputtering is the work of Bradley and Harper (BH) in which they proposed a linear continuum equation to describe the main features of ripple formation.<sup>12</sup> The main idea of BH is that smoothing and roughening processes have different wavelength dependence, leading to a preferred wavelength where the surface amplitude grows the most rapidly.

However, certain experimentally observed features, such as the saturation of the ripple amplitude and the appearance of kinetic roughening are not predicted by the linear BH theory.<sup>13,14</sup> An extension of the linear BH theory into the non-linear regime has been proposed in order to avoid these shortcomings,<sup>11</sup> resulting in a noisy version of the Kuramoto-Sivashinsky equation:

$$\frac{\partial h}{\partial t} = -v_0 + \zeta \partial_x h + \xi_x \partial_x h \partial_x^2 h + \xi_y \partial_y h \partial_y^2 h + \nu_x \partial_x^2 h + \nu_y \partial_y^2 h - K_{xx} \partial_x^4 h - K_{yy} \partial_y^4 h - K_{xy} \partial_x^2 \partial_y^2 h + \frac{\lambda_x}{2} (\partial_x h)^2 + \frac{\lambda_y}{2} (\partial_y h)^2 + \eta(x, y, t) .$$
(1)

The  $v_0$  term, which represents the average erosion rate of the unperturbed planar surface can be neglected in Eq. (1), since it does not affect the process of ripple formation. The surface height h is then in a coordinate system that moves with the average surface during the erosion process.  $\eta(x, y, t)$  is a Poisson noise term related to random fluctuations, uncorrelated in space and time, in the flux of the incoming ions.

Within this theory, ion sputtering produces periodic modulated features (correlated lat-

eral ordering) that arises from a competition of a roughening instability mechanism and surface relaxation. A roughening mechanism that often dominates the surface morphology is curvature-dependent sputtering, which is based on the linear cascade approximation first proposed by Sigmund.<sup>15</sup> However, certain compounds, such as GaSb and InP,<sup>9,16</sup> and elemental materials with refractory-metal seeding,<sup>17</sup> may also exhibit island agglomeration of excess elements by a process related to preferential sputtering.

In contrast, a wider range of relaxation mechanisms have been proposed in order to explain various experimental observations: (i) Surface diffusion (SD) mediated smoothing has been proposed to explain the temperature and ion flux dependence of ripple wavelength in the high temperature regime.<sup>2,18</sup> (ii) The surface erosion smoothing (SES) model in which higher-order terms of the erosion process produce a smoothing which mimics surface diffusion.<sup>8</sup> (iii) The ion-enhanced viscous flow relaxation (IVF) model, which considers surface-confined viscous flow driven by surface tension as the dominant smoothing mechanism for any material with a disordered surface layer with reduced viscosity.<sup>19</sup> Mayr et al. have emphasized the role of flow of point defects and of thermal-spike induced local melting in the mechanisms of radiation-induced viscous flow in the 0.1-1 KeV range.<sup>20</sup> However, determining which relaxation mechanism (SD, SES, IVF, etc.) is dominant for various amorphous or crystalline substrates, surface temperatures, and ion beam parameters, still remains the subject of vigorous research.

# II. LINEAR THEORIES

In the theoretical approach of Makeev and Barabási,<sup>11</sup> a general continuum equation which describes the evolution of surface morphology during ion sputtering is proposed. Eq. 1 incorporates the major features of ion-bombardment induced ripple formation and kinetic roughening. In the early stage of ion sputtering, Eq. (1) reduces to a BH-type linear theory when  $\lambda_x = \lambda_y = 0$ ,  $\xi_x = \xi_y = 0$ . In this article, our discussions of the wavelength tunability of ion-bombardment induced sapphire ripples are emphasized within the linear regime. The linear terms with coefficients  $\nu_x$  and  $\nu_y$  represent the curvature dependent ion erosion rates, and  $K_{xx}$  and  $K_{yy}$  are coefficients representing the surface smoothing terms.

Linear stability analysis indicates that the establishment of a periodic ripple structure across the surface depends on the balance between the curvature dependent roughening and surface smoothing mechanisms.<sup>12</sup> Two modes of rippled morphology can be induced by ion bombardment, with ripple wavevectors parallel or perpendicular to the projection of the ion beams. Regardless of the respective smoothing mechanisms (SD, SES, IVF), the wavelength of ion sputtered ripples with orthogonal orientations  $\ell_x$  (parallel) and  $\ell_y$  (perpendicular) are generally expressed as:

$$\ell_x = 2\pi \sqrt{\frac{2K_{xx}}{|\nu_x|}} \,\,\,(2)$$

$$\ell_y = 2\pi \sqrt{\frac{2K_{yy}}{|\nu_y|}} \ . \tag{3}$$

The minimum between  $\ell_x$  and  $\ell_y$  determines which orientation dominates the ion-induced ripple topography. In Eq. (2) and (3), the coefficients  $\nu_x$ ,  $\nu_y$  for curvature dependent roughening terms are given (following Ref. 11) by:

$$\nu_x = F d \frac{d_\sigma^2}{2f^3} \left\{ 2d_\sigma^4 s^4 - d_\sigma^4 d_\mu^2 s^2 c^2 + d_\sigma^2 d_\mu^2 s^2 c^2 - d_\mu^4 c^4 \right\},\tag{4}$$

$$\nu_y = -Fd \frac{c^2 d_\sigma^2}{2f} \ . \tag{5}$$

In the expressions above, the terms are defined as:

$$d_{\sigma} \equiv \frac{d}{\sigma}, d_{\mu} \equiv \frac{d}{\mu},$$

$$s \equiv \sin(\theta), c \equiv \cos(\theta),$$

$$f \equiv d_{\sigma}^{2} s^{2} + d_{\mu}^{2} c^{2},$$

$$F \equiv \frac{J \varepsilon p d}{\sigma \mu \sqrt{2\pi f}} e^{-d_{\sigma}^{2} d_{\mu}^{2} c^{2} / 2f},$$
(6)

where F is a coefficient relating to the local sputter yield  $Y(\theta)$  as:

$$F = \frac{JY(\theta)}{nc} \ . \tag{7}$$

In addition, d is the ion energy deposition depth,  $\sigma$  and  $\mu$  are ion energy distribution widths parallel and perpendicular to the incoming ion beams, J is the ion flux per area, p is a material constant depending on the surface binding energy  $U_0$  and scattering cross-section, <sup>15</sup> and n is the atomic density of the substrate.

For the SD smoothing mechanism, thermally activated surface diffusion induces surface smoothing during ion sputtering. If surface self-diffusion is isotropic, then

$$K_{xx} = K_{yy} = K_{SD} = \frac{D_s \gamma \rho}{n^2 k_B T} \ . \tag{8}$$

Here,  $D_s$  is the surface self-diffusivity, which has an Arrhenius temperature dependence  $D_s=D_0exp(-\Delta E/k_BT)$ . The surface tension (surface free energy per unit area) is  $\gamma$ , and  $\rho$  is the areal density of diffusing atoms.<sup>12</sup>

For the SES model, the erosion smoothing process is assumed to dominate over other smoothing mechanisms. Since it is not temperature dependent, it is thought to dominate at low temperatures in some cases. Here,  $K_{xx}=K_{xx,SES}$  and  $K_{yy}=K_{yy,SES}$ , which are anisotropic with respect to the direction of the incoming ion beams. The coefficients representing surface erosion smoothing  $K_{xx,SES}$  and  $K_{yy,SES}$  are given (in Ref. 11) by:

$$K_{xx,SES} = F \frac{d^3}{24} \frac{1}{f^5} \left\{ -4(3d_{\sigma}^2 s^2 f + d_{\sigma}^6 s^4) f^2 + d_{\sigma}^2 c^2 (3f^2 + 6d_{\sigma}^4 s^2 f + d_{\sigma}^8 s^4) f \right\}$$

$$+ F \frac{d^3}{24} \frac{1}{f^5} \left\{ 2(d_{\mu}^2 - d_{\sigma}^2) c^2 (15d_{\sigma}^2 s^2 f^2 + 10d_{\sigma}^6 s^4 f + d_{\sigma}^{10} s^6) \right\}, \tag{9}$$

$$K_{yy,SES} = F \frac{d^3}{24} \frac{c^2}{f} \frac{3d_{\sigma}^2}{d_{\mu}^2} \,. \tag{10}$$

For the IVF model, the ion-enhanced surface viscous flow within a thin ion-damaged layer dominates the surface smoothing. Hence,

$$K_{xx} = K_{yy} = K_{IVF} = \frac{\gamma d^3}{\eta_s} \ . \tag{11}$$

Here, the ion-enhanced surface viscosity  $\eta_s$  and the surface tension are assumed to be constant and isotropic. The depth of the damaged layer is taken to be equal to the ion penetration depth d.<sup>19</sup>

In the following sections, the data analysis and discussion of the wavelength tunability of ion-bombardment induced sapphire ripples are based on Eqs. 2-11 for the ripple wavelength. Additional smoothing mechanisms beyond SD, SES and IVF are considered in section V.

## III. EXPERIMENTAL

The ripples are produced on sapphire (0001) in a custom surface x-ray ultra-high vacuum chamber ( $10^{-9}$  torr base pressure) installed at x-ray beamline X21A1 at the National Synchrotron Light Source (NSLS) at Brookhaven National Laboratory. More details about this real-time surface x-ray characterization facility for dynamic processing are described elsewhere. In on beam sputtering is performed by either a 3-grid RF plasma ion source or a Phi model 04-192 sputter ion gun. The RF plasma ion source is operated at ion energies ranging from 300 eV to 1000 eV at a flux of  $2\times10^{14}$  ions/cm²/sec with a background Ar<sup>+</sup> pressure  $4\times10^{-4}$  torr. The irradiation size of the ion beam with a uniform flux (3 cm) is large enough to cover the entire sample surface. The Phi sputter ion gun is operated at ion energies from 500 eV to 2000 eV at a flux of  $1\times10^{13}$  ions/cm²/sec with a background Ar<sup>+</sup> pressure  $1\times10^{-4}$  torr. The sample surface temperature is adjusted from 300 K to 1050 K, and monitored by an infrared pyrometer. The chamber is also equipped with reflection high energy electron diffraction (RHEED), which is used to determine surface crystallinity. A contact mode Digital Instruments Nanoscope-E AFM is used for *ex-situ* surface morphology imaging.

The x-ray flux after the Si (111) monochromator crystal is  $2\times10^{12}$  photons/sec at a wavelength of  $\lambda=1.192$  Å with a beam-size of 0.5 mm  $\times$  0.5 mm. In the schematic representation of the x-ray measurement geometry shown in Fig. 1, the z axis is always taken to be normal to the sample surface, and the y axis along the projection of the incident x-ray beams onto the surface.  $\mathbf{k_i}$  and  $\mathbf{k_f}$  are the wave vectors of the incoming and scattered x rays, respectively. The components of the scattering momentum transfer  $\mathbf{Q} = \mathbf{k_f} - \mathbf{k_i}$  can be expressed by the glancing angles of incidence  $(\alpha_i)$  and exit  $(\alpha_f)$  with respect to the surface (x-y plane), and

the in-plane angle  $\psi$ .

In the GISAXS geometry, the incident or exit x-ray beams are fixed near the critical angle for total external reflection (0.2° for sapphire). A 320-pixel linear position sensitive detector (PSD) is positioned along x axis at the angle  $\alpha_f$  with respect to the surface, in order to collect in-plane scattered x rays. In terms of scattering momentum transfer, the PSD acquires a range of  $Q_x$  at a constant  $Q_z$  and  $Q_y$  (typically,  $Q_z$ =0.92  $nm^{-1}$ ,  $\Delta Q_x\approx 1$  nm<sup>-1</sup> and  $Q_y$ =3×10<sup>-3</sup> nm<sup>-1</sup>). Time-resolved GISAXS provides access to the evolving wavelength, shape and amplitude of surface ripples. For a full reciprocal mapping ( $Q_x$  vs.  $Q_z$ ), an  $\alpha_i = \alpha_f$  reflection mode scan is performed.

## IV. RESULTS

In this part, subsections A through D describe a series of systematic investigations of the dependance of sapphire ripple characteristics (wavelength, orientation), on experimental parameters, including ion energy, ion incidence angle and temperature.

## A. Ripple Formation by Ion Sputtering

Fig. 2 displays a  $Q_x$  vs.  $Q_z$  GISAXS scan of the rippled sapphire surface after 45° off-normal 500 eV  $Ar^+$  bombardment. First and second order satellite streaks are readily observed, indicating a periodic surface morphology along the x-direction. In this image, the specular reflected x-rays are cut off by a narrow beam stop attached to the PSD. This provides better sensitivity to off-specular diffuse scattering pattern.

Fig. 3 shows an AFM image of the as-irradiated sapphire surface. A ripple morphology is clearly visible. A wavelength of 32 nm is obtained from the image, which corresponds well with that acquired from GISAXS in Fig. 2.

Fig. 4 shows real-time GISAXS intensities plotted versus scattering momentum transfer  $Q_x$ . The scans are equivalent to a linear slice of the image in Fig. 2 at a constant vertical component of the scattering momentum transfer  $Q_z$ =0.92 nm<sup>-1</sup>, except that that an offset condition ( $\alpha_i \neq \alpha_f$ ) was used so that  $Q_y$ =3×10<sup>-3</sup> nm<sup>-1</sup>. This was done in order to eliminate the need for a specular beam stop. Scans are shown at 10-minute intervals during 45° offnormal 500 eV  $Ar^+$  bombardment. At time t=0, the initial roughness of the sapphire

surface only produces a single peak in the diffuse scattering (circles). Two satellite peaks, resulting from lateral correlated roughness become visible after 10 minutes. The ripple wavelength,  $\ell_x = 2\pi/\Delta Q_x$ , remains almost constant during ion irradiation, but the peak intensity continues to increase as a result of an increase in ripple amplitude.

It is also clear in Fig. 4 that the two satellite peaks develop in an unequal way as irradiation proceeds. After 30 minutes, the peak on the positive  $Q_x$  side is noticeably larger than the one on the negative  $Q_x$  side. At 40 minutes, the larger peak is several times more intense than the smaller one. This diffuse intensity asymmetry was also observed in the GISAXS study of ion-eroded SiO<sub>2</sub> by Umbach et al.<sup>19</sup>

Fig. 5 shows an asymmetric saw-tooth model profile, which is used as a simplified approximation to the ripple shape. Here, the parallel component of the incident ion beam is along the -x direction, as defined above. We note that the term  $\partial h/\partial x$  in Eq. (1), representing the surface local slope, has opposite signs at different sides of the solid saw-tooth. Thus, an off-normal incidence will produce different erosion rates on positive and negative slopes. The model predicts that the unbalanced erosion will make ripples move like waves across the surface in a direction opposite to the projection of the incident beam along the surface. However, we note that a recent study of ripples formed on ion-bombarded glass surfaces showed forward propagation of ripples. Nonlinear terms of the form  $(\partial h/\partial x)(\partial^2 h/\partial x^2)$  produce the asymmetric shape, which is observed in our x-ray diffuse scattering measurements. Therefore, the appearance of an asymmetric GISAXS pattern indicates the onset of this lowest order non-linear term.

# B. Ripple Wavelength Variation with Ion Energy

Fig. 6 shows the observed dependence of ripple wavelength  $\ell_x$  on ion energy  $\varepsilon$  for ion sputtered sapphire at low temperature 300 K (a) and high temperature 1000 K (b), respectively. This series of sapphire ripples are obtained at 45° off-normal ion incidence. In Fig. 6(a), square and circle symbols represent the wavelength of ripples produced by the high-flux RF plasma ion source and the low-flux ion gun, respectively. The sapphire ripple wavelength increases with ion energy at low temperature, which is consistent with observations for ion eroded SiO<sub>2</sub>, GaAs and Si surfaces. <sup>19,24,25</sup> The data obtained from high/low flux ion sources overlap within experimental error at both 500 eV and 1000 eV, which indicates that the

ripple wavelength is independent of incident ion flux at low temperature. A non-linear least squares fit gives a power law coefficient with p=0.71 for the dependence of the wavelength on ion energy ( $\ell_x \sim \varepsilon^p$ ). Also plotted are curves corresponding to p=1 and 0.5 for comparison. In Fig. 6(b), the ripple wavelength decreases with ion energy. A non-linear least squares fit gives a power law coefficient with p=-0.44. Also plotted are curves corresponding to p=-0.25 and -0.75 for comparison.

A general formula for a low temperature ripple wavelength along the dominant orientation x-axis can be expressed from Eq. (2), (4) and (9), based on the SES model (section II). Taking  $|\nu_x| \sim Fd$  and  $K_{xx,SES} \sim Fd^3$ , we can obtain the dependence of the wavelength on ion energy as:

$$\ell_x = 2\pi \sqrt{\frac{2K_{xx,SES}}{|\nu_x|}} \sim d . \tag{12}$$

The dependence of d on  $\varepsilon$  is quantitatively accessible with the aid of the ion-collison simulator SRIM.<sup>26</sup> It indicates that d varies as  $\varepsilon^p$  with p=0.48 for  $\alpha$ -sapphire at the incidence angle of 45°. The p=0.48 obtained from Eq. (12) matches the observed wavelength-ion energy relation in Fig. 6(a) reasonably well. However, a quantitative analysis (as detailed in section IV-C) by Eq. (12) predicts values of the ripple wavelengths that are an order of magnitude smaller than our measured values of  $\ell_x$ , indicating that the SES, which contains no adjustable parameters, does not account for the observed ripple wavelength at low temperature.<sup>19</sup>

A specific expression for the ripple wavelength based on the ion-enhanced surface viscous flow (IVF) model,<sup>27</sup> can be derived from Eq. (2), (4), (7) and (11) as an extension to Eq. (12). Inserting  $K_{IVF} = \gamma d^3/\eta_s$ ,  $|\nu_x| \sim Fd$  and  $F=JY(\theta)/nc$  into Eq. (2), we can get the ion energy dependence for the IVF model as:

$$\ell_x \sim 2\pi d \sqrt{\frac{2\gamma nc}{JY(\theta)\eta_s}}$$
, (13)

where the coefficient  $K_{xx}$  of the IVF smoothing term replaces  $K_{xx}$  in Eq. (2). Simulations from SRIM at 45° incidence indicate that  $Y(\theta)$  varies as  $\varepsilon^{\delta}$  with  $\delta$ =0.62. It is assumed from previous work on low energy ion irradiation<sup>28</sup> that the dependence of ion-enhanced surface viscosity on ion energy takes the form  $J\eta_s \sim \varepsilon^{-\alpha}$  with  $\alpha \approx 1$ . Hence,  $\ell_x \sim \varepsilon^p$  where p=0.67

for sapphire ripples. Here, the sapphire atomic density n is  $1.17 \times 10^{29}$  atoms/m<sup>3</sup>, the surface tension of sapphire  $\gamma$  is 0.91 J/m<sup>2</sup> (Ref. 28), and the ion flux is  $2 \times 10^{18}$  ions/m<sup>2</sup>/sec. The ion-enhanced surface viscosity  $\eta_s$  is estimated to be  $7.5 \times 10^9$  Pa-s at an ion energy of 600 eV. This value is chosen in order to give quantitative agreement between the model and the experimental values of  $\ell_x$ .

The fitted power law coefficient of p=0.71 in Fig. 6(a) and that of the IVF model (p=0.67) for the dependence of the wavelength on ion energy at low temperature are indistinguishable within experimental error. Moreover, we have observed that the RHEED pattern for the sapphire (0001) surface disappears upon ion irradiation at room temperature, confirming that ion bombardment amorphizes the surface, or at least induce a layer with a very high defect density. Similar behavior of surface amorphization under ion bombardment has been noted in the study of ion sputtered Si and InP. 16,29 The key idea of the IVF model is that this thin layer can relax by a collective motion ("flow"), driven by surface tension.

The SD model can be useful in predicting the high temperature ripple wavelength. The formula for the wavelength with its wavevector along the x-axis can be expressed from Eq. (2), (4), (7) and (8), as:

$$\ell_x \sim \sqrt{\frac{ncK_{SD}}{JdY(\theta)}}$$
, (14)

where only d and  $Y(\theta)$  are dependent on ion energy. Thus, the SD model gives  $\ell \sim \varepsilon^p$  where p=-0.55 for sapphire ripples at high temperature. The SD model is consistent with the energy dependence at high temperature in Fig. 6(b). A more refined model that combines both the IVF and SD mechanisms is given in section IV-D, which is also compatible with the data in fig. 6(b). Other variations of the SD model that include ion-bombardment effects are discussed in section V. We also note that the sapphire surface exhibits a well developed RHEED pattern after etching at 1000 K, indicating a higher degree of surface crystallinity at this temperature.

# C. Dependence of Ripple Wavelength on Ion Incidence Angle (Low Temperature)

The observed wavelength-angle phase diagram for sapphire ripples produced by 600 eV Ar<sup>+</sup> bombardment at room temperature is displayed in Fig. 7. The wavelength of sapphire

ripples is varied through a remarkably wide range (  $30 \text{ nm to } 2 \mu \text{m}$ ) by changing the incidence angle. Below  $40^{\circ}$ , the ripple wavelength is particularly sensitive to the incidence angle, while the wavelength is relatively constant in the middle range from  $40^{\circ}$  to  $65^{\circ}$ . Ion incidence at an angle larger than  $70^{\circ}$  rotates the orientation of the ripples by  $90^{\circ}$ .

The theoretical wavelength-angle phase diagram for sapphire ripples produced by 600 eV Ar<sup>+</sup> bombardment at room temperature is also shown in Fig. 7. Several variables in the expressions of Eqs. (4)-(11) were calculated using SRIM simulations, including the ion penetration depth d, the sputter yield Y( $\theta$ ), and the widths of the deposited energy distribution,  $\sigma$  and  $\mu$ . Here, the sapphire surface binding energy U<sub>0</sub> is taken to be 2 eV/atom, and the ion flux is  $2\times10^{18}$  ions/m<sup>2</sup>/sec. We estimate the ion-enhanced surface viscosity to be  $\eta_s = 7.5 \times 10^9$  Pa-s, as discussed in Section B. The predicted wavelengths  $\ell_x$  and  $\ell_y$ , based on the SES (the dash-dot line and dotted line) and IVF (the solid line and dashed line) models, are compared with those experimentally obtained.

There are three distinct regions in Fig. 7. Region I:  $\nu_x < \nu_y < 0$ ,  $K_{xx,SES} > 0$ ,  $K_{yy,SES} > 0$ ,  $K_{IVF} > 0$ . This region spans from normal incidence to oblique incidence around 62°. The ripple with wavevector parallel to the projection of the ion beam  $(\ell_x)$  dominates the surface morphology in this region. For the SES model, the  $\ell_y$  oriented ripple is predicted to dominate the morphology over most of region I, except near the region I/II boundary where the ripple orientation rotates by 90°. This is in clear disagreement with the experimental observations. On the other hand, the IVF model prediction agrees with the observed ripple orientation over the whole range. However, the IVF mechanism does not predict the observed large wavelength-angle dependence below 40°. This point will be discussed further in section V.

Region II: This region is characterized by negative  $K_{xx,SES} < 0$ , which prevents the appearance of  $\ell_x$  for the SES model, and thus the SES model predicts only  $\ell_y$  ripples in this region. In the IVF model, the  $\ell_x$  wavelength increases to infinity at the region II/III boundary near 65°. Thus, the IVF model predicts that the dominant ripples will switch their wavevector orientation to the y-direction in this region. This boundary could be adjusted towards higher angles since it is very sensitive to the change of simulated parameters, such as d,  $d_{\sigma}$  and  $d_{\mu}$ . The experimental observation is that  $\ell_x$  ripples are still observed, but longer scale order in the orthogonal direction begins to build up. Overall, the behavior in this region agrees reasonably well with the prediction of the IVF model.

Region III:  $\nu_x > 0$ ,  $\nu_y < 0$ ,  $K_{xx,SES} < 0$ ,  $K_{yy,SES} > 0$ ,  $K_{IVF} > 0$ . The  $\ell_x$  ripple is not

stable in either model, since  $\nu_x$  becomes an effective smoothing term when it is positive. Near 90°,  $\ell_y$  either drops to zero (SES) or increases to infinity (IVF). Again, the IVF model correctly predicts the observed behavior, at least qualitatively.

Ex-situ AFM images in Fig. 8 display surface morphologies obtained at different angles of incidence for ion sputtered sapphire, corresponding to the observed phase diagram in Fig. 7. Figs. 8(a) and 8(b) show images for off-normal incidence at 25°, which produces micronscale ripples with wavevector parallel to the ion beam direction, and are readily visible in the large-scale image [Fig. 8(b)]. In contrast, 55° incidence, shown in Fig. 8(c), produces a well-ordered nanorippled surface with the wavevector parallel to the projection of the incoming ion beams along the surface, which has a wavelength similar to that shown in Fig. 3. We note that at the larger scale in Fig. 8(d) the surface roughness is also correlated with wavevector perpendicular to the incoming ion beam, as predicted by  $\ell_y$  in the phase diagram. Ion incidence at 65° still creates detectable ripples with wavevector parallel to the projection of the incoming ion beams in Fig. 8(e), but obvious submicron furrows oriented along the ion beam direction are observed in Fig. 8(f). Grazing ion incidence at 75° switches the orientation of the ripple wavevector perpendicularly. Fully developed ripples are observed, with an unusual rod-like structure, as shown in Figs. 8(g) and 8(h).

## D. Temperature Dependence of Ripple Wavelength

Fig. 9 shows the observed ripple wavelength dependence on inverse temperature 1/T for two different angles of incidence. The ion energy is 600 eV for both angles of incidence. All samples are preheated to a chosen temperature and then sputtered at this temperature until a well-defined wavelength is established. The ripple wavelength obtained at 45° is constant at low temperature and increases significantly when the temperature increase over 700 K.

We have used the SD mechanism to describes the temperature dependence of the ripple wavelength at 45°. The wavelength varies as  $\ell \sim (T)^{-1/2} exp(-\Delta E/2k_BT)$ , where  $\Delta E$  is the activation energy for surface diffusion and  $k_B$  is Boltzmann's constant. However, this expression does not take into account the low-temperature component of ion bombardment induced smoothing. Thus in Fig. 9, the observed dependence of the ripple wavelength on

temperature at the incidence angle of  $45^{\circ}$  is modeled with a modified  $K_{xx}$  (solid line), as:

$$K_{xx}(\varepsilon, \theta, T) = K_{IVF}(\varepsilon, \theta) + K_{SD}(T)$$
 (15)

Taking Eq. (15) and the expression for  $K_{SD}$  in Eq. (8), we can obtain the temperature dependence of the ripple wavelength from Eq. (2). The fitting parameters are the activation energy  $\Delta E$  for surface diffusion and the areal density of mobile species  $\rho$  involving in surface diffusion. An activation energy of  $\Delta E = 0.72$  eV is extracted from Fig. 9 (solid line). Taking  $n=1.17\times10^{29}$  atoms/m<sup>3</sup>,  $\gamma=0.91$  J/m<sup>2</sup>, and assuming  $D_0$  with the order of magnitude  $10^{-8}$  m<sup>2</sup>/s, we can estimate  $\rho$  to be of the order of  $10^{13}$  m<sup>-2</sup>.

The calculated wavelengths for 35° incidence based on Eq. (2), (4), (8), (11) and (15) are shown by the dashed line in Fig. 9. A weaker, but still significant temperature dependence is predicted, which is not observed experimentally (square symbols). Rather, the experimental ripple wavelengths at 35° are independent of temperature. This indicates that the different smoothing mechanisms (i.e. thermal vs. non-thermal mechanisms) have different dependences on the angle of incidence. In particular, the rapid increase in wavelength at low angles is inferred to be due to a non-thermal smoothing mechanism that increases at low angles to dominate over the other mechanisms, but is not included in our present model.

Finally, Fig. 10 shows the observed wavelength-angle phase diagram ( $\ell_x$  vs.  $\theta$ ) for sapphire ripples obtained at two temperatures, 300 K and at 1000 K. The theoretical curves based on Eq. (2), (4), (8), (11) and (15) are also plotted. The solid line for 300 K is identical to the solid line in Fig. 7, which is just based on the IVF model. The dashed line for 1000 K includes both SD and IVF smoothing effects, combined as shown in Eq. (15). We note that the experimental ripple wavelength  $\ell_x$  exhibits a very large increase and is not sensitive to thermal activation for incidence angles below 40°. Taken together, these observations again indicate a strong non-thermal smoothing mechanism which is not adequately explained by any of the models under consideration.

# V. DISCUSSION

The observations in the section IV-B and IV-C indicate that the IVF and SD models fits some of the trends of the wavelength dependence on experimentally accessible parameters. However, some of the characteristics during the ripple formation are beyond the current theories as described in sections IV-C and IV-D. Fig. 7 shows that the obtained wavelength for incidence angle lower than 40° spans a range of two orders of magnitude from 30 nm to 2  $\mu$ m. Figs. 8(c) and 8(d) confirm that ion incidence at 25° only produces surface features at the larger scale. Furthermore, ion sputtering at normal incidence does not roughen the surface at all from the onset of irradiation, which is confirmed by a real-time GISAXS study. This is in contrast to the theoretical behavior which predicts that the ripple wavelength only increases slightly as normal incidence is approached. If the nonlinear terms  $\lambda_x$  and  $\lambda_y$  are introduced into the continuum equation describing the surface motion, kinetic roughening is expected in the region I of the phase diagram (when  $\lambda_x \cdot \lambda_y > 0$ ), but such roughening is not observed. These unusual effects lead us to propose that there is an additional smoothing mechanism that dominates the behavior near normal incidence.

We have considered the fact that the theoretical ripple wavelength is very sensitive to the ion range d, so that a small (factor of two) uncertainty in d would have a large (order of magnitude) effect on the calculated wavelength for certain models. A factor that is not taken into account in SRIM simulations is the ion-channeling effect.<sup>30</sup> Ion channeling in crystalline surface layers would be strongest near low-index crystallographic directions, and could potentially lead to an increase in ion range d near the [0001] axis, and a corresponding increase in ripple wavelength. Based on RHEED analysis of sapphire surfaces after ion bombardment at different temperatures, there is a striking increase in surface order at higher substrate temperatures, and we would expect a stronger channeling effect for the experiments at high temperatures than at low temperatures. However, Fig. 10 does not show any effect of temperature at the lowest angles of incidence, effectively refuting this idea. Furthermore, the cutoff of ion-channeling by a low energy threshold in the range between 0.1-1 keV may weaken its possible influence on the formation of erosion patterns.<sup>31</sup>

Another important factor that is not taken into consideration by current models to explain surface morphology created by ion sputtering is ion impact induced lateral mass redistribution.<sup>4,32,33</sup> It can induce a form of surface smoothing process that is different from the SD, SES or IVF relaxation mechanisms previously discussed. Impact-induced downhill currents have been identified as the driving force underlying the ultra-smoothness of surfaces resulting from ion assisted film deposition.<sup>33</sup> The ion induced lateral currents gives rise to curvature dependent  $(\partial^2 h/\partial x^2, \partial^2 h/\partial y^2)$  smoothing terms, which can weaken or even cancel the curvature dependent roughening term in Eq. (1) [see Eq. (6) in Ref. 4]. No ripples can

form under conditions where this type of smoothing term is dominant, since the wavelength dependence exactly matches that of the prevailing roughening mechanism. Thus, the idea that this additional smoothing mechanism plays a role at low angles of incidence provides a route which may explain the anomalous wavelength-angle phase diagram in Figs. 7 and 10. We also note that the lateral current term is expected to be strongest at low angles of incidence.<sup>4</sup>

The behavior of the ripple formation at high temperature can be explained reasonably by the SD model. However, another important fact observed in our experiments, but not discussed above, is that thermal annealing at 1000 K without ion irradiation does not produce any distinguishable decay of the amplitude of as-prepared ripples, in contrast with previous studies on Si and Ag surfaces.<sup>34,35</sup> This indicates that the surface smoothing at high temperature is not by a type of surface diffusion that is purely thermally activated. Rather, it is likely to involve to the creation of mobile species on the surface during ion bombardment. Further work on the flux dependence of the  $\ell_x$  at high temperature will assist us in clarifying the dominant creation process for mobile species underlying the ion-enhanced surface diffusion.<sup>2</sup>

#### VI. SUMMARY

In summary, the formation and characteristics of ripple morphologies on sapphire surfaces produced by ion sputtering are systematically investigated by in-situ GISAXS and ex-situ AFM. The ripple wavelength can be modulated effectively in a wide range of 20 to 2000 nm by changing the ion incidence angle, ion energy and temperature. This phenomenon provides an easy route to fabricate nanostructured surfaces for exploring novel nanoscale phenomenon. The IVF and SD smoothing mechanisms are shown to play an important role in the formation of the sapphire ripple structure. The possible importance of impact-induced lateral currents as a smoothing mechanism should also be investigated further.

## ACKNOWLEDGMENTS

We wish to acknowledge the experimental assistance and facility supports of Dr. Lin

Yang from NSLS-X21 and Prof. Jie Yang from the UVM physics department. This material is based upon work supported by the National Science Foundation under Grant No. 0348354 and by the Department of Energy under Grant No. DEFG0203ER46032.

- \* Electronic address: rheadrick@uvm.edu
- <sup>1</sup> U. Valbusa, C. Boragno, and F. Buatier de Mongeot, J. Phys.: Condens. Matter 14, 8153 (2002).
- <sup>2</sup> J. Erlebacher, M. J. Aziz, E. Chason, M. B. Sinclair, and J. A. Floro, Phys. Rev. Lett. 82, 2330 (1999).
- <sup>3</sup> E. Chason, T. M. Mayer, B. K. Kellerman, D. T. McIlroy, and A. J. Howard, Phys. Rev. Lett. **72**, 3040 (1994).
- <sup>4</sup> G. Carter and V. Vishnyakov, Phys. Rev. B. **54**, 17647 (1996).
- D. Datta, S. R. Bhattacharyya, T. K. Chini, and M. K. Sanyal, Nucl. Instr. and Meth. in Phys. Res. B 193, 596 (2002).
- <sup>6</sup> S. Rusponi, C. Boragno, and U. Valbusa, Phys. Rev. Lett. **78**, 2795 (1997).
- <sup>7</sup> R. Cuerno and A. L. Barabási, Phys. Rev. Lett. **74**, 4746 (1995).
- <sup>8</sup> M. A. Makeev and A. L. Barabási, Appl. Phys. Lett. **71**, 2800 (1997).
- <sup>9</sup> S. Facsko, T. Dekorsy, C. Koerdt, C. Trappe, H. Kurz, A. Vogt, and H. L. Hartnagel, Science 285, 1551 (1999).
- R. Moroni, D. Sekiba, F. Buatier de Mongeot, G. Gonella, C. Boragno, L. Mattera, and U. Valbusa, Phys. Rev. Lett. 91, 167207 (2003).
- <sup>11</sup> M. A. Makeev, R. Cuerno, and A. L. Barabási, Nucl. Instr. and Meth. in Phys. Res. B 197, 185 (2002).
- <sup>12</sup> R. M. Bradley and J. M. E. Harper, J. Vac. Sci. Technol. A **6**, 2390 (1988).
- <sup>13</sup> J. Erlebacher, M. J. Aziz, E. Chason, M. B. Sinclair, and J. A. Floro, J. Vac. Sci. Tech. A 18, 115 (2000).
- <sup>14</sup> E. A. Eklund, R. Bruinsma, J. Rudnick, and R. S. Williams, Phys. Rev. Letts **67**, 1759 (1991).
- <sup>15</sup> P. Sigmund, Phys. Rev. **184**, 383 (1969).
- <sup>16</sup> F. Frost, A. Schindler, and F. Bigl, Phys. Rev. Lett. **85**, 4116 (2000).
- <sup>17</sup> G. Ozaydin, A. Ozcan, Y. Y. Wang, F. K. Ludwig, H. Zhou, R. L. Headrick, and D. P. Siddons, Appl. Phys. Lett. 87, 163104 (2005).
- <sup>18</sup> S. W. MacLaren, J. E. Baker, N. L. Finnegan, and C. M. Loxton, J. Vac. Sci. Tech. A **10**, 468 (1992).

- <sup>19</sup> C. C. Umbach, R. L. Headrick, and K. C. Chang, Phys. Rev. Lett. **87**, 246104 (2001).
- <sup>20</sup> S. G. Mayr, Y. Ashkenazy, K. Albe, and R. S. Averback, Phys. Rev. Lett. **90**, 055505 (2003).
- <sup>21</sup> A. S. Ozcan, G. Ozaydin, Y. Wang, K. F. Ludwig, R. L. Headrick, H. Zhou, and D. P. Siddons (unpublished).
- O. Malis, J. D. Brock, R. L. Headrick, M.-S. Yi, and J. M. Pomeroy, Phys. Rev. B 66, 035408 (2002).
- <sup>23</sup> P. F. A. Alkemade, Phys. Rev. Letts **96**, 107602 (2006).
- <sup>24</sup> A. Karen, Y. Nakagawa, M. Hatada, K. Okuno, F. Soeda, and A. Ishitani, Surf. Interface Anal. 23, 506 (1995).
- <sup>25</sup> J. J. Vajo, R. E. Doty, and E. H. Cirlin, J. Vac. Sci. Technol. A **14**, 2709 (1996).
- <sup>26</sup> J. F. Ziegler, J. P. Biersack, and U. Littmark, Stopping and Range of Ions in Solids (Pergamon Press, New York, 1985).
- <sup>27</sup> S. E. Orchard, Appl. Sci. Res. **11A**, 451 (1962).
- <sup>28</sup> T. M. Mayer, E. Chason, and A. J. Howard, J. Appl. Phys. **76**, 1633 (1994).
- <sup>29</sup> S. Hazra, T. K. Chini, M. K. Sanyal, J. Grenzer, and U. Pietsch, Phys. Rev. B 70, 121307(R) (2004).
- <sup>30</sup> L. C. Feldman, J. W. Mayer, and S. T. Picraux, Materials Analysis by Ion Channeling (Academic Press, New York, 1982).
- <sup>31</sup> G. Hobler, Nucl. Instr. and Meth. in Phys. Res. B **115**, 323 (1996).
- <sup>32</sup> H. Johnson, N. Kalyanasundaram, B. Davidovitch, M. Brenner, M. J. Aziz, and J. Freund, APS Bulletin 51, 294 (2006).
- <sup>33</sup> M. Moseler, P. Gumbsch, C. Carsiraghi, A. C. Ferrari, and J. R. Lieb, Science **309**, 1545 (2005).
- <sup>34</sup> J. Erlebacher, M. J. Aziz, E. Chason, M. B. Sinclair, and J. A. Floro, Phys. Rev. Lett. 84, 5800 (2000).
- <sup>35</sup> L. Pedemonte, G. Bracco, C. Boragno, F. B. de Mongeot, and U. Valbusa, Phys. Rev. B. 68, 115431 (2003).

# Figure Captions

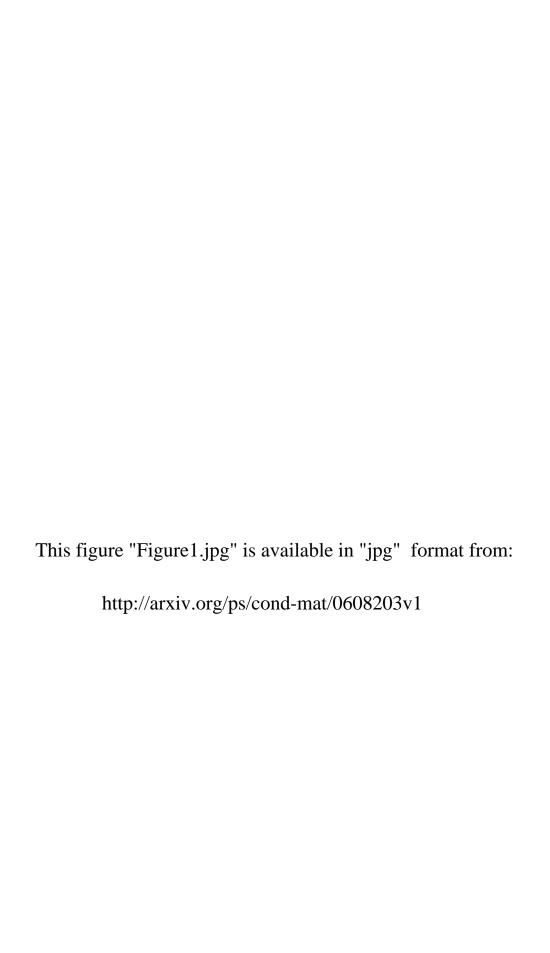
- FIG 1. Schematic of the x-ray scattering geometry. The z-axis is always taken to be normal to the sample surface, and the incident x-ray beam defines the y-z plane.  $\mathbf{k_i}$  and  $\mathbf{k_f}$  represent the incident and scattered wave vectors, respectively. The components  $(\mathbf{Q}_x, \mathbf{Q}_y)$  and  $\mathbf{Q}_z$  of the scattering momentum transfer  $\mathbf{Q} = \mathbf{k_f} \mathbf{k_i}$  are defined by the glancing angles  $\alpha_i$ ,  $\alpha_f$  and in-plane (x-y plane) angle  $\psi$ . The linear PSD is oriented with its long direction in the plane of the surface.
- FIG 2. Grazing incidence small angle x-ray scattering (GISAXS) patterns acquired from  $Q_x$ - $Q_z$  scans. Asymmetric GISAXS patterns indicate the shape anisotropy on the ripples. The bar of gray shades represents the logarithmically scaled intensity.
- FIG 3. A 500 nm by 500 nm AFM image taken after the GISAXS measurements. The ripple wave vector is parallel to the projected ion beam direction. In the text, this is referred to as the  $\ell_x$  orientation of ripples.
- FIG 4. Time-resolved GISAXS measurements indicate the increase of the lateral correlations on a sapphire surface during ion exposure. The surface ripples are produced by 500 eV Ar<sup>+</sup> bombardment at 45° incidence. The vertical component of the scattering momentum transfer  $Q_z$  was fixed at 0.92 nm<sup>-1</sup> and  $Q_y$  was offset to  $3 \times 10^{-3}$  nm<sup>-1</sup>.
- FIG 5. An asymmetric saw-tooth model profile ( $\alpha < \beta$ ). The parallel component of the incident ion beam along the substrate surface is along the -x direction, as defined in Fig. 1. The term  $\partial h/\partial x$  represents the local slope of ion etched surface curvature. The magnitude of  $\alpha$  and  $\beta$  are exaggerated for clarity.
- FIG 6. The dependence of the ripple wavelength ( $\ell_x$ ) of ion etched sapphire on the incident ion energy ( $\varepsilon$ ). (a) 300 K substrate temperature. The square symbols are for the high flux ion source and the circle symbols are for the low flux ion source. The solid line is the curve for the best fit exponent of p=0.71. For comparison, curves for p=1 and p=0.5 are plotted as dashed and dotted lines, respectively. (b) 1000 K substrate temperature. The solid line is for the best fit exponent of p=-0.44. For comparison curves for p=-0.25 and p=-0.75 are plotted as dashed and dotted lines, respectively.
- FIG 7. The wavelength-angle phase diagram for sapphire ripples produced by 600 eV Ar<sup>+</sup> bombardment. Circle symbols: experimental wavelength  $\ell_x$  at room temperature. Square symbol: experimental wavelength  $\ell_y$  at room temperature (Only one point at 75° is shown). The error bars are comparable to the height of the symbols. Two sets of curves are shown:

The upper set is for the IVF model, with the solid line representing the simulated  $\ell_x$  wavelength, and the dashed line representing the  $\ell_y$  wavelength. The lower set of curves is for the SES model, where the dot-dashed line represents the  $\ell_x$  wavelength and the dotted line represents the  $\ell_y$  wavelength. Experimentally, the three regions of the phase diagram represent the ranges of angles where  $\ell_x$  and  $\ell_y$  are dominant (I and III, respectively), and a narrow transition region (region II). The SES model predicts that  $\ell_y$  ripples dominate in all three regions, which is not consistent with the data. The IVF model gives better agreement with the data, as described in the text.

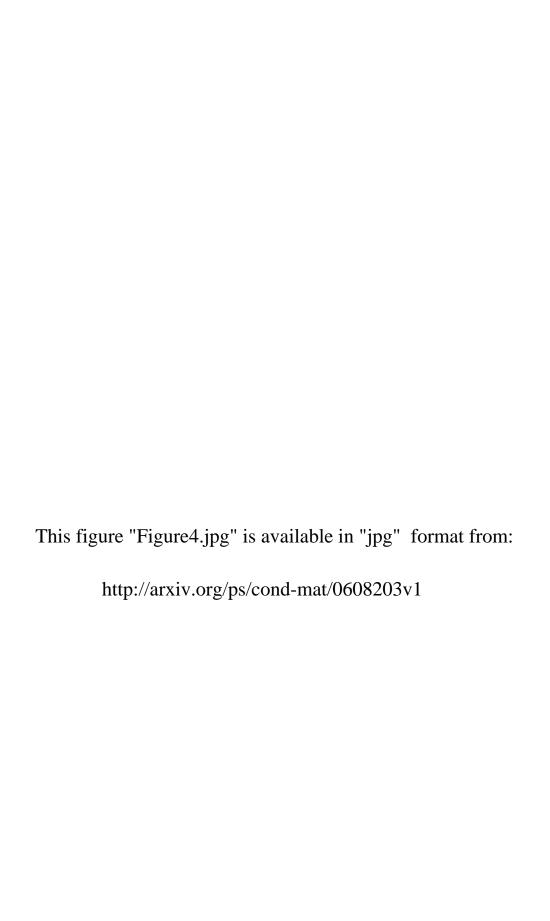
FIG 8. AFM images of surface morphology at different angles of incidence: (a) and (b) are for an incidence angle of 25°, (c) and (d) are for an incidence angle of 55°, (e) and (f) are for an incidence angle of 65°, and (g) and (h) are for an incidence angle of 75°. Two different image sizes are shown for each angle of incidence. The white arrow indicates the projection of the ion beam direction along the surface. The progression of ripple orientation and wavelength can be seen in this sequence of images. In particular, we note the large scale ripples at 25° in (b), followed by much smaller wavelength ripples at 55° in (c) and 65° in (e), and finally the rotation of the ripple orientation in (g) and (h).

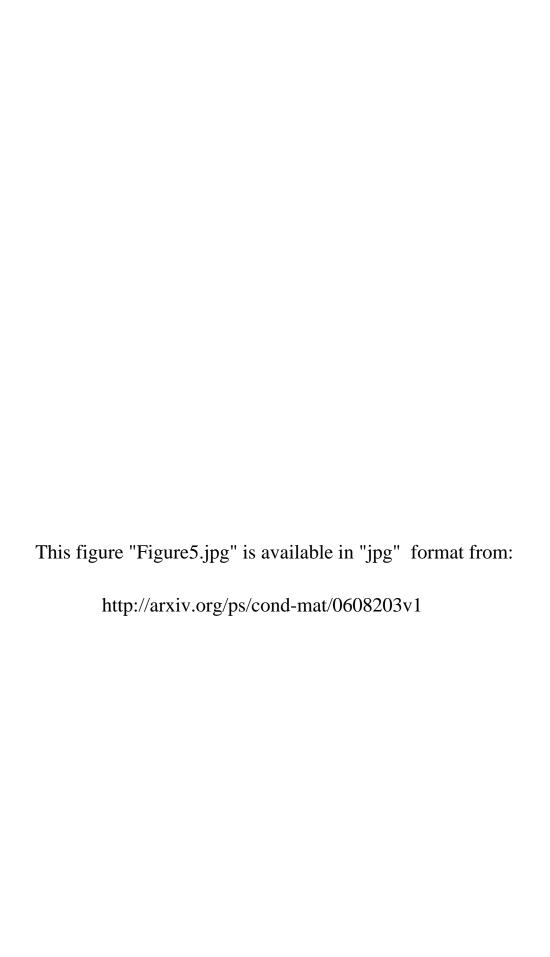
FIG 9. The wavelength  $\ell_x$  as a function of inverse temperature at different angles of incidence and constant ion energy of 600 eV. Theoretical curves based on Eqs. (2), (4), (8), (11) and (15) are shown for the set of ripples wavelength  $\ell_x$  obtained at incidence angles of 35° (dash line) and 45° (solid line) off-normal incidence.

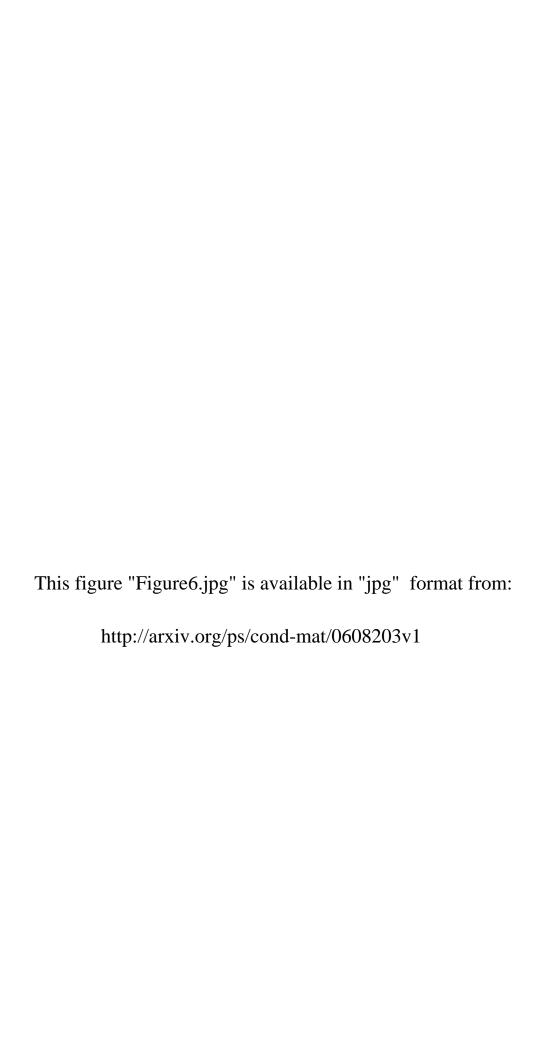
FIG 10. The wavelength-angle phase diagram for sapphire ripples produced by 600 eV  $Ar^+$  bombardment at different temperatures. The error bars are comparable to the height of the symbols. The curves for  $\ell_x$  based on Eqs. (2), (4), (8), (11) and (15) are compared with the measured ripples wavelengths obtained at 300 K (solid line) and 1000 K (dash line), respectively.



This figure "Figure2.jpg" is available in "jpg" format from: http://arxiv.org/ps/cond-mat/0608203v1 This figure "Figure3.jpg" is available in "jpg" format from: http://arxiv.org/ps/cond-mat/0608203v1







This figure "Figure7.jpg" is available in "jpg" format from: http://arxiv.org/ps/cond-mat/0608203v1

